ACTUATORS

Untethered soft robotic matter with passive control of shape morphing and propulsion

Arda Kotikian[1]*, Connor McMahan[2]*, Emily C. Davidson[1], Jalilah M. Muhammad[1], Robert D. Weeks[1], Chiara Daraio[2†], Jennifer A. Lewis[1†]

There is growing interest in creating untethered soft robotic matter that can repeatedly shape-morph and self-propel in response to external stimuli. Toward this goal, we printed soft robotic matter composed of liquid crystal elastomer (LCE) bilayers with orthogonal director alignment and different nematic-to-isotropic transition temperatures (T_{NI}) to form active hinges that interconnect polymeric tiles. When heated above their respective actuation temperatures, the printed LCE hinges exhibit a large, reversible bending response. Their actuation response is programmed by varying their chemistry and printed architecture. Through an integrated design and additive manufacturing approach, we created passively controlled, untethered soft robotic matter that adopts task-specific configurations on demand, including a self-twisting origami polyhedron that exhibits three stable configurations and a "rollbot" that assembles into a pentagonal prism and self-rolls in programmed responses to thermal stimuli.

INTRODUCTION

Soft robots are versatile in ways that rigid systems are not. Their compliant nature allows them to safely interact with living organisms (*1*, *2*) and fragile objects (*2*, *3*). They can perform complex motions as a result of simple actuation inputs (*4*–*6*), conform to arbitrary geometries (*7*), perform multigait propulsion (*8*), morph into different shapes (*8*, *9*), and withstand large deformation or impact without damage (*10*). However, challenges associated with the integration of untethered, fully soft actuation modalities currently limit their broader utilization. To date, soft robots have primarily relied on pneumatic networks embedded within elastomeric matrices for actuation and propulsion (*2*, *6*, *8*, *11*). Yet, most pneumatically actuated soft robots must be tethered to rigid power and control systems to generate sufficient forces for locomotion (*6*, *12*). Recently, active matter that self-actuates in response to external and internal stimuli (e.g., temperature, light, chemical gradients, and electric fields) has been explored as an alternative for soft robots (*5*, *13*–*20*). However, active materials also have limitations that must be overcome. For example, electroactive actuators must be tethered to rigid power sources (*19*, *20*), shape-memory polymers require manual reprogramming (*17*, *21*, *22*), bilayer strips made of materials that undergo differential growth are volumetrically expensive (*18*, *23*, *24*), and hydrogel-based actuators must be paired with pneumatic systems to produce large forces quickly (*1*, *25*).

The creation of untethered, soft robots that perform complex tasks is difficult. For example, pneumatically actuated soft robots typically undergo large deformations across their entire structural frame (*8*, *10*). Predicting the kinematics of these systems is not straightforward because nonlinear elastic models that satisfy a diverse set of boundary conditions are required. These challenges are compounded when the implementation of control systems is desired. Origami-based strategies offer a compelling alternative for designing soft robots that exhibit large shape changes through a reduced set of predictable motions. One can greatly simplify the design space by localizing deformations to creases within the robotic structure, e.g., using actuating hinges connected to planar facets. Recently, reconfigurable robots with rigid on-board power sources and electronic controls have been constructed by this method (*26*–*29*).

Soft robots may also benefit from hinge-based actuation, in which compliant, energy-dense actuators are placed at creases, whereas stiffer structural elements serve as planar facets (*30*). Folding patterns can be modeled and predicted geometrically using existing mathematical tools (*31*–*33*). The design and implementation of controls in origami-based untethered systems can be achieved solely through the constitutive response of the actuating hinges, and locomotive gaits can be encoded within their frames via programmable folding sequences. Although controlled folding sequences have been realized in rigid and hybrid (soft/rigid) systems (*26*, *34*), fully soft systems implemented to date are typically irreversible (*17*, *22*, *35*), geometrically constrained (*36*), or tethered to rigid power sources (*18*, *37*). New advances are needed to generate untethered soft robots that exhibit repeatable actuation (*38*), self-morphing (*25*), and self-propulsion in response to external stimuli (*39*).

Liquid crystal elastomers (LCEs) have recently emerged as a promising class of soft active matter because they generate large, powerful, and repeatable deformations upon heating above their nematic-to-isotropic transition temperature (T_{NI}) (*40*, *41*). The direction of contractile strain (director) can be programmed by aligning rigid mesogens during fabrication (*40*, *41*). In addition to thermal stimuli, LCEs that respond to electric (*42*), light (*43*, *44*), or chemical stimuli (*13*, *45*) have been synthesized. However, despite their remarkable behavior, LCEs have not been widely integrated within untethered robotic structures because of fabrication challenges that relegate them to simple unidirectional actuators (*40*) or voxelated thin films (~50 μm thick) (*45*, *46*). Current LCEs are either too compliant to support large loads or lack the capability to output large torques in compact, untethered arrangements (*18*, *47*–*49*). Recent attempts to achieve LCE-based untethered locomotion have relied on using small-scale actuators that are not integrated with other functional components (*14*–*16*, *50*). Recently, voxelated LCEs have been produced in thick-film geometries (~1 mm thick) via three-dimensional (3D) printing (*51*–*53*). These 3D LCEs actuate reversibly and exhibit large

---

[1]John A. Paulson School of Engineering and Applied Sciences, Wyss Institute of Biologically Inspired Engineering, Cambridge, MA 02138, USA. [2]Division of Engineering and Applied Science, California Institute of Technology, Pasadena, CA 91125, USA.
*These authors contributed equally to this work.
†Corresponding author. Email: daraio@caltech.edu (C.D.); jalewis@seas.harvard.edu (J.A.L.)

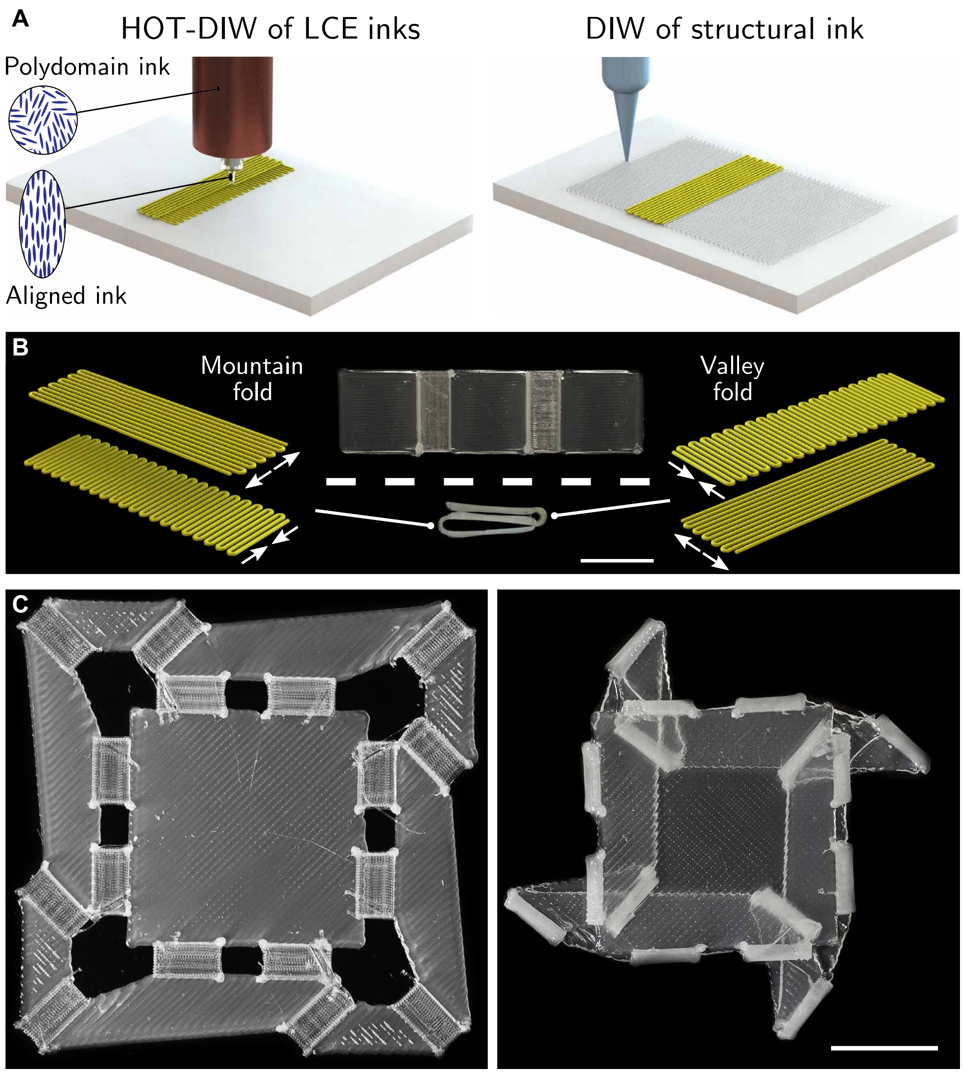

Fig. 1. 3D printing of soft robotic matter. (**A**) Active hinges were printed from oligomeric LCE inks, whose rigid mesogens aligned along the print path during HOT-DIW (left). Immediately upon printing, LCE ink cross-linking was photo-initiated to lock in the desired director alignment. Structural tiles were then printed from an ink composed of acrylate resin that chemically bonded to LCE hinges upon photo-initiated cross-linking (right). (**B**) The LCE hinges were printed in the form of 0°/90° and 90°/0° bilayers, which bend into mountain and valley folds, respectively, when actuated above T_{NI}. A simple structure composed of two hinges, with mountain and valley folds, that interconnect three structural tiles is shown as printed (middle and top) and as actuated (middle and bottom). (**C**) A more complex, square-twist reconfigurable structure was printed (left) and actuated at 125°C (right). The LCE hinges that form the central square and the four LCE hinges that point toward the center of the structure (left) are mountain folds, whereas the other LCE hinges are valley folds. Scale bars, 1 cm.

work capacities. However, the ability to combine multiple LCE actuators with programmed director alignment with soft structural materials has not yet been demonstrated in a single-step fabrication process.

Here, we created untethered, soft robotic matter that can reversibly shape-morph and propel itself in response to thermal stimuli. Specifically, we printed LCE hinges that interconnect structural polymeric tiles to produce active architectures that exhibit large, repeatable deformations. Using this method, the folding orientation, hinge angles, and actuator geometry are fully programmable. By incorporating LCEs with two different T_{NI}, we created soft robotic matter that exhibits sequential folding and unfolding in response to different temperatures. Through an integrated design and manufacturing method, we demonstrated simple embodiments of origami-inspired soft robots, whose shape morphing and self-propulsion were passively controlled via the constitutive response of the printed matter. As an exemplar, we produced an origami-based architecture that could adopt three different stable configurations, depending on its exposure to varying thermal conditions. Next, we characterized the mechanical response of the active LCE hinges, which generated a torque capable of folding and lifting objects that were more than two orders of magnitude heavier than the hinges themselves. Last, we exploited their torque response to create a printed (flat) structure that was reconfigured to a pentagonal prism and propelled itself by rolling on a hot surface, which we refer to as a "rollbot."

RESULTS

Printing soft active hinges and structural tiles

The active hinges and structural tiles were fabricated as shown in Fig. 1. All inks were formulated with the desired viscoelastic behavior needed to facilitate direct ink writing (fig. S1) (*54*). The hinges were composed of LCE bilayers that exhibit orthogonally programmed nematic order, which interconnect each structural tile. Two oligomeric LCE inks were synthesized with low and high T_{NI} values of 24° and 94°C and are referred to as LT_{NI} and HT_{NI} inks, respectively. Such differences arise because of disparities in their backbone flexibility and cross-linking chemistry (fig. S2). The LT_{NI} ink was composed of a thiol-terminated liquid crystalline oligomer and trivinyl-functionalized cross-linker (*52*), whereas the HT_{NI} ink was composed of an acrylate-terminated liquid crystalline oligomer analogous to previously reported inks composed of main-chain mesogens (Fig. 2A) (*45*, *51*, *53*, *55*). To ensure strong adhesion between the printed hinges and tiles, we used a structural ink for printing the tiles that was composed of a photopolymerizable diacrylate resin and an acrylate cross-linker that chemically binds to the reactive LCE groups. The ink rheology was modified by adding fumed silica to achieve the desired yield stress and a shear thinning behavior needed for printing (fig. S1).

The LCE inks were printed using high operating temperature direct ink writing (HOT-DIW) (*51*). To facilitate director alignment during printing, we printed the LT_{NI} ink at 26°C and the HT_{NI} ink at 50° to 55°C (fig. S1) (*51*). Ink cross-linking was photo-initiated immediately upon printing to lock in the programmed director alignment along

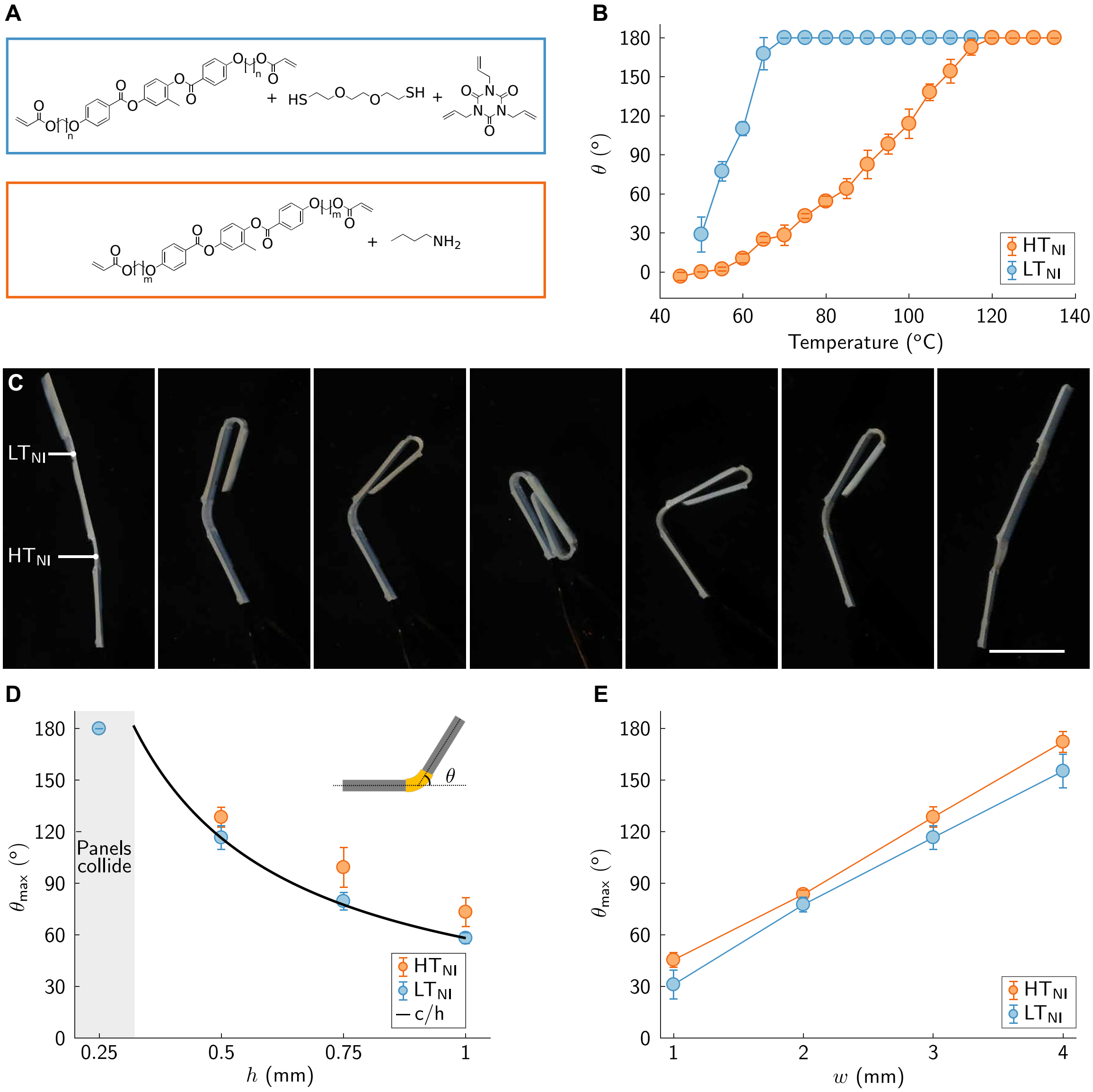

Fig. 2. Untethered, sequential, and reversible folding of active hinges. (**A**) Chemical composition of the LT_{NI} (blue) and HT_{NI} (orange) oligomeric LCE inks (where $n = 3$ and 6, and $m = 6$ in the molecular structures). (**B**) Bending angle θ as a function of temperature for LT_{NI} and HT_{NI} LCE hinges with length of 10 mm, width of 4 mm, and thickness of 0.25 mm. (**C**) A printed structure composed of LT_{NI} and HT_{NI} LCE hinges with mountain folds that interconnect three structural tiles, which undergo sequential actuation when heated (left to center) and cooled (center to right). Scale bar, 1 cm. (**D**) Bending angle θ as a function of thickness, *h*, for LT_{NI} and HT_{NI} LCE hinges of fixed length of 10 mm and width of 3 mm. Their bending angle decreased with thickness. Other bilayer systems display inverse proportionality between curvature and thickness (*57*–*59*). We plot this relationship, where *c* is a constant, for comparison. Both hinges exhibited a maximum bending angle of 180°, where panels contact one another. (**E**) Bending angle θ as a function of hinge width, *w*, for LT_{NI} and HT_{NI} LCE hinges of fixed length of 10 mm and thickness of 0.5 mm. Error bars indicate SD.

the print path (fig. S3). After printing and cross-linking, the low T_{NI} LCE structures became fully isotropic at 92°C, and high T_{NI} LCE structures did so at 127°C (*51*, *53*), enabling these structures to sequentially actuate in response to thermal stimuli. We note that LCE actuation can occur over a wide temperature range (*52*). Unidirectionally printed HT_{NI} LCE films (0.375 mm thick) exhibited a repeated contraction of −49.8 ± 0.9% along the printing direction and an expansion of 41.7 ± 5.7% perpendicular to that direction, whereas the LT_{NI} LCEs exhibited respective values of −31.1 ± 0.6% and 21.5 ± 0.6% (fig. S4). The structural tiles were printed under ambient conditions via DIW. The placement of each structural tile induced a bending axis that is parallel to the LCE hinge interface (Fig. 1A, right). Upon curing, the printed tiles exhibited a stiffness of 766 ± 41 MPa, which provided the structural integrity to prevent collapse of the printed architectures under self- and applied loading conditions.

To achieve controlled bending, we fabricated each LCE hinge in a "bilayer" design, in which the bottom half is composed of multiple layers printed along the same direction and the top half is composed of multiple layers printed in the orthogonal direction (Fig. 1A, left). A spontaneous strain mismatch caused each hinge to bend when heated above their actuation temperature. We chose an orthogonal bilayer design because the spontaneous strains in each layer favored a single bending direction around a given axis. Consequently, greater curvatures were achieved compared with bilayer hinges composed

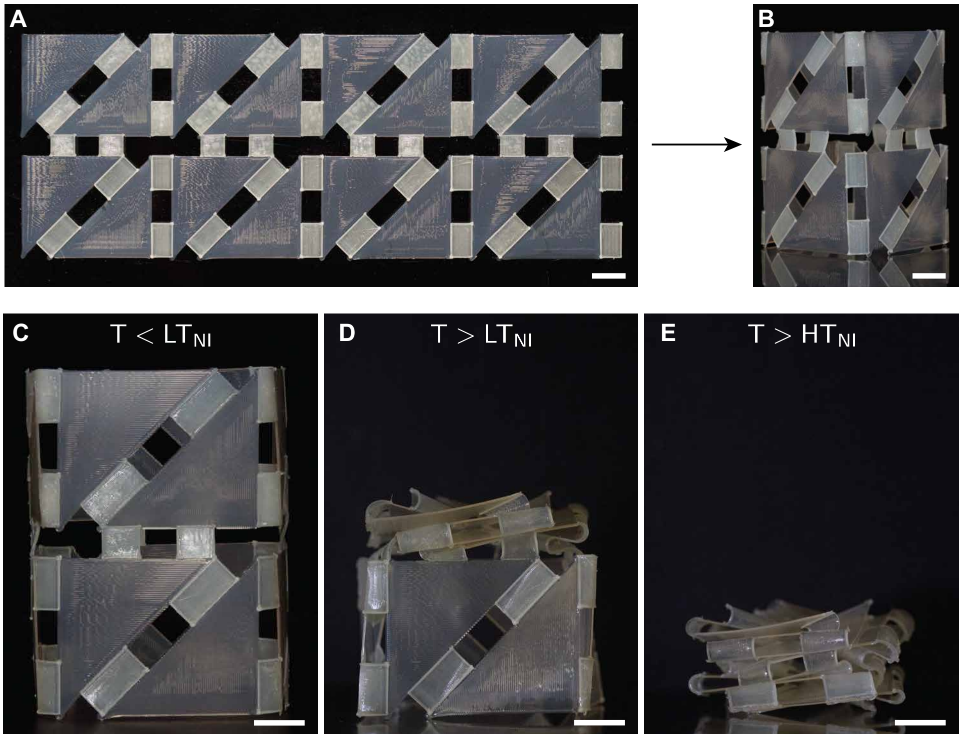

Fig. 3. Printed soft robotic matter with programmed sequential folding and deformation. (**A**) A triangulated polyhedron was printed in the form of a flat sheet composed of both LT_{NI} hinges (top section) and HT_{NI} hinges (bottom section) that interconnect the structural tiles. All diagonal LCE hinges are valley folds, whereas all vertical and horizontal LCE hinges are mountain folds. (**B**) The printed flat sheet was manually assembled into a 3D triangulated structure that exhibited sequential folding upon heating from (**C**) ambient temperature to (**D**) 100°C, where the LT_{NI} LCE hinges actuated, and to (**E**) 150°C, where the HT_{NI} LCE hinges actuated. Scale bars, 1 cm.

of a top LCE layer and a bottom inactive layer (*47*, *48*). The folding orientation of each LCE hinge is defined by the print path. The bilayer (bottom/top) orientation relative to the printing direction determines whether they exhibit mountain (0°/90°) or valley (90°/0°) folds (Fig. 1B). Because self-folding is reversible, the printed structures could be repeatedly actuated by cycling above and below their respective actuation temperatures. To demonstrate this, we printed both mountain and valley hinges in a simple structure composed of two LCE hinges that interconnected three structural tiles, as shown in Fig. 1B (center), which repeatedly folded and unfolded without manual intervention. By varying the specific arrangement of active hinges and structural tiles, we could realize more complex self-folding structures, including the square twist unit cell shown in Fig. 1C (movie S1). In both cases, the architectures contained hinges printed using a single LCE ink (HT_{NI}). Below, we demonstrate the broad versatility that arose from the integration of multiple LCE hinges of different T_{NI} values with structural tiles.

Programmed sequential self-folding

Sequential self-folding is essential for untethered origami-inspired structures because this capability enables collision prevention during shape morphing and locomotive gaits with multiple degrees of freedom triggered by distinct stimuli (*30*, *35*). By printing LCE inks with different actuation temperatures, we created soft robotic matter with programmable sequential folding upon heating (Fig. 2A). The unbiased bending angle (where hinges do not bear a load) increases with temperature for both LT_{NI} and HT_{NI} LCE hinges. From direct observations, we found that both the onset and the completion of folding for the LT_{NI} LCE hinges occur at considerably lower temperatures, relative to their HT_{NI} counterparts (Fig. 2B). Specifically, the LT_{NI} LCE hinges begin to fold below 40°C, whereas the onset of folding occurs near 60°C for HT_{NI} LCE hinges. Because of the residual stress that arose from cross-linking the LT_{NI} LCE hinges in their isotropic phase (*56*), these hinges had a negative bending angle under ambient conditions (fig. S5). Although both types of hinges could achieve a 180° folding angle, their temperature response depended strongly on their composition and overall dimensions (figs. S5 and S6). Leveraging these capabilities, we printed a simple structure that integrated both LT_{NI} and HT_{NI} LCE mountain hinges, which interconnected three structural tiles and sequentially actuated when heated (Fig. 2C). As expected, the LT_{NI} LCE hinge folded completely before the HT_{NI} LCE hinge actuated. The structure unfolded in reverse upon cooling to room temperature; i.e., the HT_{NI} LCE hinge unfolded to its flat configuration first, followed by the LT_{NI} LCE hinge. This demonstration highlights our ability to create soft robotic matter with programmed sequential folding in untethered motifs (movie S2).

Folding temperatures were programmed by the LCE chemistry, and hinge angles were prescribed geometrically by the printing process. We defined the hinge length and width as the in-plane geometric parameters in the directions parallel and perpendicular to the folding axis, respectively. The hinge thickness was defined in the surface normal direction and varied in discrete increments of 0.25 mm, which corresponds to twice the nozzle diameter used during HOT-DIW. By varying the number of printed layers, we produced hinges with thicknesses between 0.25 mm (one layer in each direction) and 1 mm (four layers in each direction). The spontaneous curvature that the actuators assume at temperatures above T_{NI} decreased with hinge thickness (Fig. 2D), akin to other bilayer systems (*57*–*59*). We discuss the LCE hinge mechanics in further detail in the Supplementary Materials. HT_{NI} LCE hinges exhibited greater unbiased folding angles compared with LT_{NI} LCE hinges of identical geometry, because the strain differential between directions parallel and perpendicular to their director alignment is more pronounced (*57*, *58*). For a given hinge thickness, the folding angle increased proportionally with the hinge width (Fig. 2E) because the curvature remained constant when their width was varied. Our additive manufacturing approach is both scalable and flexible, so there is no limit on the hinge thickness or geometry. However, the director was misaligned near each edge of the LCE hinges, where the printing nozzle changed direction in a semicircular arc to enable continuous printing of adjacent-aligned filaments. Hence, because of this effect, the minimum LCE hinge width must exceed two nozzle diameters (in this case, 0.25 mm). We note that the minimum hinge width also

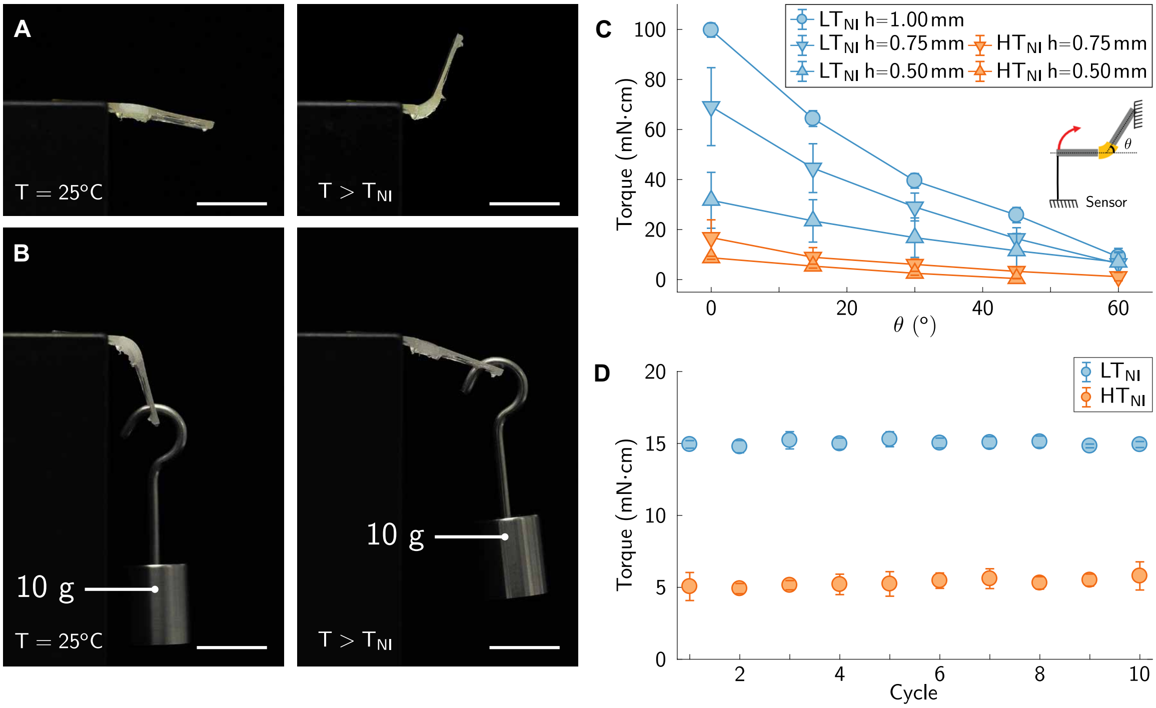

Fig. 4. Torque capacity of printed active hinges. (**A**) LT_{NI} LCE hinge (10 mm by 4 mm by 1 mm) folds to a 75° bending angle while unbiased. (**B**) When a 10-g mass was suspended 1 cm away from the LCE hinge at room temperature, it deflected to −72°. The mass was lifted by about 1 cm when actuated above T_{NI}. (**C**) Exerted torque as a function of hinge folding angle, θ, as defined by the inset. Hinge composition and thickness, *h*, are the primary factors that affect torque output. (**D**) LCE hinges (5 mm by 3 mm by 0.5 mm) undergo multiple actuation cycles with negligible changes in the torque output. Error bars indicate SD. Scale bars, 1 cm.

increased with LCE thickness because the misalignment radius increased when LCE layers were printed on top of one another compared with those printed directly on the underlying glass substrate. This misalignment caused hinges programmed as valley folds to have marginally smaller bending angles compared with those programmed as mountain folds. This is because their top layer is parallel to hinge width, which is a smaller in-plane geometric parameter than hinge length (fig. S7). The printed LCE hinges could bend repeatedly without bias weight, and their maximum folding angle remained constant over multiple heating and cooling cycles (fig. S8). Their repeatable actuation is an essential feature for untethered soft robotic applications that operate without manual intervention.

Next, we demonstrate that soft robotic matter can be designed and printed with geometric locking mechanisms. As one example, we created the triangulated polyhedron shown in Fig. 3, which is based on a well-known origami design (*60*). The structure was printed in a planar layout (Fig. 3A) before manually joining the edges (Fig. 3B) to create an open polyhedron that was stable at room temperature (Fig. 3C). The top and bottom sections of the polyhedron were identical, except that different LCE inks were used to print their respective hinges. Specifically, the top section contained LT_{NI} LCE hinges that facilitated folding into a compacted form when heated above 95°C. The bottom section contained HT_{NI} LCE hinges that remained unfolded when the top layer actuated (Fig. 3D) yet compact when heated above 155°C (Fig. 3E and movie S3). An environment temperature well above the T_{NI} of both materials was used to accelerate the folding process. All hinges were constructed with a 6-mm width and 0.5-mm thickness to ensure 180° folding angles upon actuation. This geometry was stable after each intermediate folding stage, even when the structure returned to room temperature (fig. S9). This behavior is similar to what was observed in paper origami structures that locked in intermediate folding states due to bending of the facets between two flat-faceted states (*60*, *61*). Guest and Pellegrino (*60*) provided a good overview of these multistable geometries and their kinematics. The observed behavior (fig. S9) for these printed structures suggests that a variety of multistable architectures can be created by our approach.

Programmed self-propulsion

Untethered self-propulsion is a requirement for autonomous and preprogrammed robotic systems that navigate large distances in uncertain environments (*21*). This poses challenges, especially given that untethered operation often requires onboard power and control systems that add mass to the robot (*25*, *62*). LCE bilayers offer a promising option for these tasks because they are energy dense and are capable of performing multiple loading and unloading cycles in response to external stimuli. However, because of the inherently soft nature of LCE hinges, large external moments induce bending and lead to actuated hinge angles that are different from the unloaded hinge measurements (Fig. 2). As an example, a printed LT_{NI} LCE hinge achieved a 79° bending angle when unbiased (Fig. 4A), but when a 10-g mass was suspended 1 cm away from the hinge at room temperature, it deflected to −72° because of its compliance. When heated above T_{NI}, the hinge bent by 55°, and the mass was lifted 6.5 mm (Fig. 4B), corresponding to a work output of about 0.6 mJ. This actuation is remarkable for a soft actuator with dimensions 10 mm by 3 mm by 1 mm. It corresponds to an energy density of 29 J/kg when accounting for the combined mass (22 mg) of the

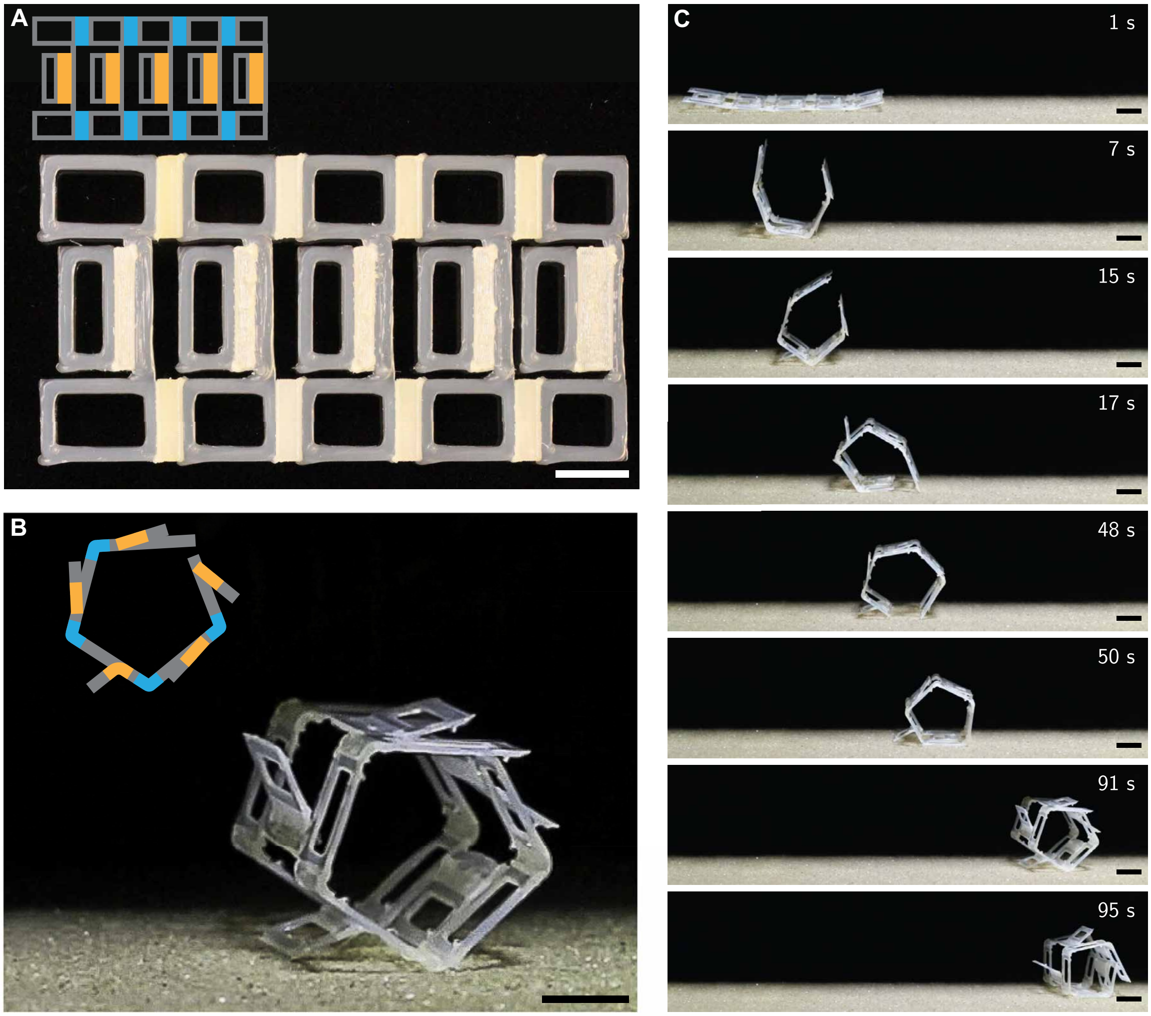

Fig. 5. Printed self-propelling structure. (**A**) Self-propelling rollbot is shown in its printed configuration. In the legend (inset), the blue (LT_{NI}) and orange (HT_{NI}) LCE hinges denote valley and mountain folds, respectively, and gray indicates structural tiles. (**B**) Printed structure in its rolling configuration, in which the LT_{NI} LCE hinges induced folding into a pentagonal prism and the HT_{NI} LCE hinges propelled the rollbot when heated above their actuation temperature. (**C**) Still images (from movie S4) of the rollbot that show its self-propelling locomotion when heated. The structure self-propels at least six times over the time sequence shown. [The heated surface was held at 200°C, and the average ambient temperature was 45°C. Scale bars, 1 cm.]

LCE hinge and structural panels, which is in good agreement with our earlier work (*51*). The mass of the lifted object was more than 450 times greater than the hinge mass.

We quantified the torque output of LCE bilayer hinges to further explore their suitability for reconfigurable and propulsive soft robots. Both types of LCE hinges were tested in different geometries. For a given thickness, LT_{NI} LCE hinges output more torque than their HT_{NI} counterparts (Fig. 4C). Torque increases with hinge thickness for both LCE chemistries but diminishes with increasing folding angle. Consequently, heavier self-assembling and self-propelling structures will require hinges that are capable of greater torque outputs because hinges will only fold until there is equilibrium between external moments and their curvature-dependent torque capacity. Torque output remained constant over multiple heating and cooling cycles (Fig. 4D), which is essential for repeatable propulsion in untethered robots. We noticed an asymmetry in the torque produced by the actuators when heated compared with the relatively lower restoration torque exerted by hinges during cooling. This asymmetry is disadvantageous for applications that require large torque outputs in both rotational directions but leads to energy savings in deployable structures that require a permanent post-actuated configuration, such as the printed structure shown in Fig. 3, which remained locked in a post-actuated configuration rather than unfolding under ambient conditions.

We exploited the large torque output by the printed LCE hinges to achieve passive control of self-assembly and propulsion in a rolling architecture (i.e., rollbot) (Fig. 5). The entire structure was printed flat with a total mass of 1.67 g. The structural frame was composed of two outer rails that use LT_{NI} LCE hinges to morph from a flat state (Fig. 5A) to a pentagonal prism with edge lengths of 15 mm (Fig. 5B). These rails were connected by bridges that hold propelling HT_{NI} LCE hinges. A hot plate held at an average surface temperature of 200°C and a convective environment that sustains the ambient temperature at 45°C were used to passively induce the desired assembly and rolling motion. Under these conditions, the LT_{NI} LCE hinges actuated to a ~72° hinge angle and remained folded throughout the rolling process because of the modest difference between their T_{NI} and the ambient temperature, even away from the hot plate. The actuated LT_{NI} hinges provided enough torque to allow the structure to maintain a pentagonal shape during rolling, obviating the need for a locking mechanism. A free-body analysis was used to determine the torque requirements for shape reconfiguration and propulsion (fig. S10). To transform into a pentagonal prism, the LT_{NI} LCE hinges must have a minimum torque output of 9.9 mN·cm at a 0° hinge angle (flat configuration) and a sustained torque of 0.3 mN·cm when fully folded (fig. S11). Given these torque and angle requirements, we printed LT_{NI} LCE hinges with a width of 4 mm and a thickness of 0.75 mm. In the assembled 3D configuration, the HT_{NI} LCE hinges actuated when in contact with the hot plate, rolling the structure over the adjacent vertex and onto the next hinge, which carried out the same action. Propelling the structure over vertices required a 36° tipping angle, and the corresponding torque needed to initiate this action was 6.9 mN·cm exerted by the hinge (fig. S11). To realize this, we printed HT_{NI} LCE hinges that were 2 mm wide and 0.50 mm thick as propelling actuators. These hinges were also printed with a 4-mm offset from the tipping vertex to provide mechanical advantage. Because of this offset, HT_{NI} LCE hinges must fold by 63°. A greater hinge angle was needed for tipping over an open vertex, so 4-mm HT_{NI} LCE hinges were used for propulsion over a small gap. Both LT_{NI} and HT_{NI} LCE hinge dimensions were chosen on the basis of the torque measurements described above, and a pentagonal frame was selected to showcase the torque capabilities of LCE hinges (rolling over vertices requires large torque outputs). Because these hinges unfolded away from the hot surface, their repeated actuation was possible. This allowed temperature gradient-driven propulsion to continue even after the structure completed a full roll without a need for manual reprogramming, traveling ~12 cm in 95 s (Fig. 5C and movie S4). This simple concept can be expanded upon to passively control soft robotic matter and, ultimately, robots with more sophisticated reversible functions and locomotive gaits.

DISCUSSION

We have demonstrated a design and additive manufacturing method for integrating LCE bilayer actuators, into shape-morphing and self-propelling structures. We integrated programmable LCE hinges that actuate at different temperatures. The orthogonal orientation of these bilayer hinges induces anticlastic bending (i.e., saddle-like surfaces) and reduces their bending energy (*49*). Even so, torque outputs are large enough for lifting objects that are substantially heavier than the hinges themselves and, importantly, for self-propulsion. We envision that given the modular nature of these inks, it would be relatively straightforward to incorporate LCEs that respond to other stimuli (e.g., light, pH, and humidity) within these printed architectures. Through the introduction of multiple stimuli-responsive actuators and more complex folding sequences, we can further expand the functionality of untethered soft robotic systems capable of task-specific reconfiguration and locomotion.

MATERIALS AND METHODS

Ink synthesis and characterization

The LT_{NI} ink was synthesized by a previously reported thiol-acrylate "click" reaction (*52*). As-received 2,2′-(ethylenedioxy)diethanethiol (Sigma-Aldrich), 1,4-bis-[4-(6-acryloyloxy-hexyloxy)benzoyloxy]-2-methylbenzene (Wilshire Technologies Inc.), 1,4-bis-[4-(3-acryloyloxypropypropyloxy) benzoyloxy]-2-methylbenzene (Matrix Scientific), and 1,3,5-triallyl-1,3,5-triazine-2,4,6(1H,3H,5H)-trione (Sigma-Aldrich) in a mole ratio of 1.0:0.6:0.2:0.133, and 1 weight % (wt %) triethylamine (Sigma-Aldrich), 2 wt % butylated hydroxytoluene (Fisher Scientific), and 1.5 wt % Irgacure 651 (BASF) were melted and mixed in an amber scintillation vial with a heat gun (MHT3300, Milwaukee) and vortexed for about 5 min. The reaction was subsequently heated and stirred for 3 hours at 65°C in an oil bath. The HT_{NI} ink was synthesized by a previously reported aza-Michael addition method (*51*). A 1.1:1 mole ratio of 1,4-bis-[4-(6-acryloyloxyhexyloxy) benzoyloxy]-2-methylbenzene and *n*-butyl amine (Sigma-Aldrich), 0.2 wt % butylated hydroxytoluene, and 2 wt % Irgacure 651 were added to a 25-ml round-bottom flask fitted with a condenser. The reaction was stirred at 105°C for 18 hours while protecting it from ambient fluorescent light.

The structural ink was prepared by mixing Ebecryl 8413 resin (Allnex) and pentaerythritol tetraacrylate (TCI Chemicals) in a 1:1 weight ratio with 10 wt % fumed silica (CAB-O-SIL EH-5, Cabot) and 4 wt % Irgacure 651. Irgacure 651 was added as a solution in dichloromethane (Sigma-Aldrich) at a concentration of 750 mg/ml. After each reagent was added, the ink was mixed in a SpeedMixer (FlackTek Inc.) for about 3 min. The solvent was evaporated before printing. An Instron tensile testing machine was used to measure the stiffness of dogbone-shaped structural tiles.

The respective T_{NI} of each oligomeric LCE ink was determined by differential scanning calorimetry (DSC) measurements (TA Q200 calorimeter). Uncross-linked LCE ink samples (10 to 15 mg each) were hermetically sealed inside TZero aluminum pans. Samples were analyzed via a heat-cool-heat cycle between −50° and 150°C with ramp rates of 10°C/min to clear the thermal history on the first heating ramp and to access both the glass transition temperatures and nematic-to-isotropic transition temperatures of the inks. Samples were held isothermally for 1 min at both high and low temperatures. Data from the second heating ramp were analyzed to determine their T_g and T_{NI} values.

The rheological properties of inks were measured using a controlled-stress rheometer (Discovery HR-3 Hybrid Rheometer, TA Instruments) equipped with a 20-mm peltier plate geometry with a 250-μm gap. Before each test, LCE inks were brought to 100°C, then to testing temperature for 300 s to erase structural history of the inks during the loading process. During the viscometry measurements, shear rate was swept from 0.001 to 1000 s^{-1}. During the oscillatory measurements, stress was swept from 0.01 to 1000 Pa at 1 Hz. The rheological properties of the elastomeric ink used to pattern the structural tiles were measured using a 40-mm cone geometry under ambient conditions. During the viscometry measurements, the ink viscosity was measured as the shear rate was swept from 0.0001 to 10,000 s^{-1}. During the oscillatory measurements, its storage and loss moduli were determined by carrying out stress sweeps from 0.0001 to 10,000 Pa at 1 Hz.

Alignment of printed LCE samples was characterized by x-ray scattering measurements on a SAXSLAB system with a Rigaku 002 microfocus x-ray source (λ = 1.5409 Å) with a sample-to-detector (PILATUS 300K) distance of 109 mm to capture the mesogen-mesogen correlations at $q \sim 1.5$ Å^{-1}. Wide-angle x-ray scattering samples consisted of two-layer printed LCE unidirectional strips (200 to 250 μm thick). Samples were exposed for 300 s. Data reduction was performed using the Nika Macro for Igor Pro. Herman's orientational order parameter $<P_2>$ was calculated by extracting the intensity of the mesogen scattering peak as a function of azimuthal angle, masking low-intensity regions due to the beamstop and gaps in the PILATUS 300K detector and then using a custom MATLAB script. The order parameters of printed LT_{NI} and HT_{NI} LCEs are 0.1707 and 0.2688, respectively.

Unbiased linear actuation of unidirectional LCE as a function of temperature was determined by increasing temperature at 4°C min^{-1} with a programmable heating stage (modified HCS302, Instec) on 20 mm–by–5 mm–by–0.375 mm unidirectional samples from 25° to 150°C. The stage was covered in a thin layer of silicone oil to enhance heat transfer and reduce friction. Images were collected from above every 15 s via a Canon EOS Rebel T2i camera with a Canon 100-mm macro lens, and dimensions were analyzed via ImageJ.

Fabrication and operation of programmed soft robotic matter

LCE hinges were printed using a customized HOT-DIW printhead (operating at $T < 100$°C). The printhead composed of a machined copper block that was designed to couple to a Nordson 3-cc high-pressure adapter (Nordson EFD). For heating control, a resistance temperature detector sensor in the block (Omega) monitored the temperature adjacent to the nozzle, two 100-W ¼–by–2 in cartridge heaters (Omega) in the copper block provided heating, and a Teflon mounting block provided insulation. Feedback control was provided via an Omega platinum series single-zone temperature controller. The LCE inks were loaded into a custom SS 3-cc syringe with a 250-μm nozzle (TecDia Inc.). LT_{NI} and HT_{NI} inks were printed at 26°C and 50° to 55°C and at print speeds of 25 and 28 mm s^{-1}, respectively. Both were printed at a print height of 0.125 mm, a filament spacing of 0.125 mm, and a pressure of 455 psi using a 3-cc high-pressure adapter controlled with a pressure box (Ultimus V, Nordson EFD). On-the-fly ultraviolet (UV) curing (OmniCure S2000) was carried out at 20,000 μW cm^{-2} for LT_{NI} LCE ink and 8000 μW cm^{-2} for HT_{NI} LCE ink. Structural tiles were printed by extruding the ink through a 410-μm tapered nozzle (Nordson EFD) at an average speed of 30 mm s^{-1}, a print height of 0.25 mm, a filament spacing of 0.2 mm, and a pressure of 60 psi (Ultimus V, Nordson EFD). Inks were printed using our multimaterial 3D printer (customized ABG 10000, Aerotech Inc.) and G-Code (MeCode). All samples except the shape-morphing element and self-propelling structure were printed on an untreated glass slide (VWR). The triangulated polyhedron and the self-propelling structure were printed on a sacrificial polyvinyl alcohol (99% hydrolyzed; Sigma-Aldrich)–coated glass substrate. After printing, all samples were cross-linked upon exposure to UV light (6000 μW cm^{-2}) for about 15 min per side.

The triangulated polyhedron was fully printed in a single step in a flat configuration. The 3D configuration was achieved by bonding the edges of outlying LCE hinges to structural tiles with the structural ink. All hinges in the structure were 0.5 mm thick and 6 mm wide. The triangulated polyhedron was actuated in two steps. First, it is placed in an oven at 100°C to actuate the LT_{NI} LCE hinges. Next, it was placed in an oven at 155°C to actuate the HT_{NI} LCE hinges (Fig. 4 and movie S3). After each actuation in the sequence, the structure was imaged at room temperature (fig. S9).

The self-propelling structure (Fig. 5) was printed with LT_{NI} LCE hinges that were 0.75 mm thick and 4 mm wide and HT_{NI} LCE hinges that were 0.5 mm thick and 2 mm wide. The last HT_{NI} LCE hinge that propels the structure at the open vertex of the pentagonal prism was 0.5 mm thick and 4 mm wide. The self-propelling structure was tested on a substrate with a sand-covered silicone adhesive (Rutland). The substrate was heated with a hotplate to have a surface temperature of about 200°C. To provide a heated and convective environment, we placed a space heater (Sunbeam) 4 in away and set at 27°C. To ensure a thin boundary layer of heat at sand surface, we used a fan. Both the convective heater and the fan were aligned to be parallel to the self-propelling structure.

Characterization of programmed soft robotic matter

Images of actuated samples in Fig. 1 (B and C) and movie S1 were taken in an oil bath with a temperature of 125°C acquired from above. The sample in Fig. 4 (A and B) was heated with a heat gun (MHT3300, Milwaukee) until the sample was optically clear, indicating full actuation. All unbiased folding angle measurements were conducted by printing one stiff panel longer than the other to fit in an acrylic holder perpendicular to the panel face. Hinges were printed as mountain folds unless otherwise specified. The hinges were inverted into an oil bath of the temperature of measurement and imaged from above with a camera (Canon EOS 5D Mark III). For repeatable bending measurements (fig. S8), hinges were alternated between room temperature and a hot oil bath. For LT_{NI} and HT_{NI} LCE hinges, the oil bath was at 120° and 150°C, respectively. Images were taken after 30 s in the hot oil bath and after 2 min at room temperature. Sequential folding images (Fig. 2C and movie S2) were taken from above, as samples were heated from room temperature to 150°C in an oil bath and cooled passively to room temperature again. The edges of all hinges analyzed for bending angle were colored black with permanent marker (Sharpie) to enhance contrast for image analysis (MATLAB). All images analyzed for bending angle were taken using a Canon EOS 5D Mark III camera from above.

To measure their torque output, we fixed one of the LCE hinges' structural panels to a rotary stage that was used to control hinge angle. The second panel was attached to a thin string 10 mm away from the edge of the LCE. The string, with negligible bending stiffness, was axially stiff and was fixed to a force sensor at the other end. A linear stage was used in conjunction with the near-inextensible string for fine-tuning the target hinge angle, ensuring that the force vector being measured by the sensor was normal to the second hinge panel and to the sensor plate. The actuators were heated using a 24-W metal ceramic heater (Thorlabs Inc.), causing them to bend away from the sensor until reaching the target hinge angle. At this target angle, the string experienced axial forces, which were measured by a Mettler Toledo XS205 scale. The measured force plateaued with the completion of the nematic-to-isotropic phase transition. Torque cycling experiments were carried out at a 0° hinge angle by turning the heater off upon reaching full actuation. See fig. S12 for images of the experimental setup and fig. S13 for additional torque measurements.

SUPPLEMENTARY MATERIALS

robotics.sciencemag.org/cgi/content/full/4/33/eaax7044/DC1
Text S1. Mechanics of thin nematic elastomer bilayers.
Fig. S1. LCE and structural tile ink rheology.
Fig. S2. DSC curves for the LCE inks.
Fig. S3. LCE alignment.
Fig. S4. Actuation response of unidirectional printed LCEs.
Fig. S5. Bending angle as a function of temperature.
Fig. S6. Bending angle as a function of hinge dimensions.
Fig. S7. Valley fold bending angles.
Fig. S8. Repeatable hinge folding.
Fig. S9. Triangulated polyhedron actuation sequence at ambient temperature.

Fig. S10. Free-body diagrams of self-propelling rollbot.
Fig. S11. Torque requirements of hinges for self-propelling rollbot.
Fig. S12. Torque measurement experimental setup.
Fig. S13. Torque measurements for hinges of varied dimensions.
Movie S1. Actuation of square twist origami unit.
Movie S2. Reversible, sequential actuation of hinges.
Movie S3. Actuation sequence of triangulated polyhedron.
Movie S4. Passively controlled propulsion of soft robot.

REFERENCES AND NOTES

1. H. Yuk, S. Lin, C. Ma, M. Takaffoli, N. X. Fang, X. Zhao, Hydraulic hydrogel actuators and robots optically and sonically camouflaged in water. *Nat. Commun.* **8**, 14230 (2017).
2. F. Ilievski, A. D. Mazzeo, R. F. Shepherd, X. Chen, G. M. Whitesides, Soft robotics for chemists. *Angew. Chem. Int. Ed.* **50**, 1890–1895 (2011).
3. B. T. Phillips, K. P. Becker, S. Kurumaya, K. C. Galloway, G. Whittredge, D. M. Vogt, C. B. Teeple, M. H. Rosen, V. A. Pieribone, D. F. Gruber, R. J. Wood, A dexterous, glove-based teleoperable low-power soft robotic arm for delicate deep-sea biological exploration. *Sci. Rep.* **8**, 14779 (2018).
4. F. Connolly, C. J. Walsh, K. Bertoldi, Automatic design of fiber-reinforced soft actuators for trajectory matching. *Proc. Natl. Acad. Sci. U.S.A.* **114**, 51–56 (2017).
5. E. Hawkes, B. An, N. M. Benbernou, H. Tanaka, S. Kim, E. D. Demaine, D. Rus, R. J. Wood, Programmable matter by folding. *Proc. Natl. Acad. Sci. U.S.A.* **107**, 12441–12445 (2010).
6. M. Wehner, R. L. Truby, D. J. Fitzgerald, B. Mosadegh, G. M. Whitesides, J. A. Lewis, R. J. Wood, An integrated design and fabrication strategy for entirely soft, autonomous robots. *Nature* **536**, 451–455 (2016).
7. J. R. Amend, E. Brown, N. Rodenberg, H. M. Jaeger, H. Lipson, A positive pressure universal gripper based on the jamming of granular material. *IEEE Trans. Robot.* **28**, 341–350 (2012).
8. R. F. Shepherd, F. Ilievski, W. Choi, S. A. Morin, A. A. Stokes, A. D. Mazzeo, X. Chen, M. Wang, G. M. Whitesides, Multigait soft robot. *Proc. Natl. Acad. Sci. U.S.A.* **108**, 20400–20403 (2011).
9. W. Hu, G. Z. Lum, M. Mastrangeli, M. Sitti, Small-scale soft-bodied robot with multimodal locomotion. *Nature* **554**, 81–85 (2018).
10. M. T. Tolley, R. F. Shepherd, B. Mosadegh, K. C. Galloway, M. Wehner, M. Karpelson, R. J. Wood, G. M. Whitesides, A Resilient, untethered soft robot. *Soft Robot.* **1**, 213–223 (2014).
11. K. Suzumori, S. Endo, T. Kanda, N. Kato, H. Suzuki, A bending pneumatic rubber actuator realizing soft-bodied manta swimming robot, in *Proceedings of the 2007 IEEE International Conference on Robotics and Automation (ICRA)* (IEEE, 2007), pp. 4975–4980.
12. N. W. Bartlett, M. T. Tolley, J. T. B. Overvelde, J. C. Weaver, B. Mosadegh, K. Bertoldi, G. M. Whitesides, R. J. Wood, A 3D-printed, functionally graded soft robot powered by combustion. *Science* **349**, 161–165 (2015).
13. Y. Liu, B. Xu, S. Sun, J. Wei, L. Wu, Y. Yu, Humidity- and photo-induced mechanical actuation of cross-linked liquid crystal polymers. *Adv. Mater.* **29**, 1604792 (2017).
14. S. Palagi, A. G. Mark, S. Y. Reigh, K. Melde, T. Qiu, H. Zeng, C. Parmeggiani, D. Martella, A. Sanchez-Castillo, N. Kapernaum, F. Giesselmann, D. S. Wiersma, E. Lauga, P. Fischer, Structured light enables biomimetic swimming and versatile locomotion of photoresponsive soft microrobots. *Nat. Mater.* **15**, 647–653 (2016).
15. C. Ahn, K. Li, S. Cai, Light or thermally powered autonomous rolling of an elastomer rod. *ACS Appl. Mater. Interfaces* **10**, 25689–25696 (2018).
16. A. H. Gelebart, D. Jan Mulder, M. Varga, A. Konya, G. Vantomme, E. W. Meijer, R. L. B. Selinger, D. J. Broer, Making waves in a photoactive polymer film. *Nature* **546**, 632–636 (2017).
17. Q. Ge, C. K. Dunn, H. J. Qi, M. L. Dunn, Active origami by 4D printing. *Smart Mater. Struct.* **23**, 094007 (2014).
18. C. Yuan, D. J. Roach, C. K. Dunn, Q. Mu, X. Kuang, C. M. Yakacki, T. J. Wang, K. Yu, H. J. Qi, 3D printed reversible shape changing soft actuators assisted by liquid crystal elastomers. *Soft Matter* **13**, 5558–5568 (2017).
19. N. Kellaris, V. Gopaluni Venkata, G. M. Smith, S. K. Mitchell, C. Keplinger, Peano-HASEL actuators: Muscle-mimetic, electrohydraulic transducers that linearly contract on activation. *Sci. Robot.* **3**, eaar3276 (2018).
20. A. O'Halloran, F. O'Malley, P. McHugh, A review on dielectric elastomer actuators, technology, applications, and challenges. *J. Appl. Phys.* **104**, 071101 (2008).
21. T. Chen, O. R. Bilal, K. Shea, C. Daraio, Harnessing bistability for directional propulsion of soft, untethered robots. *Proc. Natl. Acad. Sci. U.S.A.* **115**, 5698–5702 (2018).
22. J. Wu, C. Yuan, Z. Ding, M. Isakov, Y. Mao, T. Wang, M. L. Dunn, H. J. Qi, Multi-shape active composites by 3D printing of digital shape memory polymers. *Sci. Rep.* **6**, 24224 (2016).
23. Q. Zhang, K. Zhang, G. Hu, Smart three-dimensional lightweight structure triggered from a thin composite sheet via 3D printing technique. *Sci. Rep.* **6**, 22431 (2016).
24. C. Wang, K. Sim, J. Chen, H. Kim, Z. Rao, Y. Li, W. Chen, J. Song, R. Verduzco, C. Yu, Soft Ultrathin Electronics Innervated Adaptive Fully Soft Robots. *Adv. Mater.* **30**, 1706695 (2018).
25. S. I. Rich, R. J. Wood, C. Majidi, Untethered soft robotics. *Nat. Electron.* **1**, 102–112 (2018).
26. S. Felton, M. Tolley, E. Demaine, D. Rus, R. Wood, A method for building self-folding machines. *Science* **345**, 644–646 (2014).
27. D. Rus, M. T. Tolley, Design, fabrication and control of origami robots. *Nat. Rev. Mater.* **3**, 101–112 (2018).
28. J.-S. Koh, K.-J. Cho, Omega-shaped inchworm-inspired crawling robot with large-index-and-pitch (LIP) SMA spring actuators. *IEEE ASME Trans. Mechatron.* **18**, 419–429 (2013).
29. W. P. Weston-Dawkes, A. C. Ong, M. R. A. Majit, F. Joseph, M. T. Tolley, Towards rapid mechanical customization of cm-scale self-folding agents, in *2017 IEEE/RSJ International Conference on Intelligent Robots and Systems* (IROS, 2017), pp. 4312–4318.
30. X. Ning, X. Wang, Y. Zhang, X. Yu, D. Choi, N. Zheng, D. S. Kim, Y. Huang, Y. Zhang, J. A. Rogers, Assembly of advanced materials into 3D functional structures by methods inspired by origami and kirigami: A review. *Adv. Mater. Interfaces* **5**, 1800284 (2018).
31. R. J. Lang, A computational algorithm for origami design, in *Proceedings of the 12th Annual ACM Symposium on Computational Geometry* (ACM, 1996), pp. 98–105.
32. T. Tachi, Freeform variations of origami. *J. Geom. Graph.* **14**, 203–215 (2010).
33. E. D. Demaine, T. Tachi, Origamizer: A practical algorithm for folding any polyhedron, in *Proceedings of the 33rd International Symposium on Computational Geometry* (SoCG 2017), pp. 34:1–34:15.
34. S. Miyashita, S. Guitron, S. Li, D. Rus, Robotic metamorphosis by origami exoskeletons. *Sci. Robot.* **2**, eaao4369 (2017).
35. Y. Liu, B. Shaw, M. D. Dickey, J. Genzer, Sequential self-folding of polymer sheets. *Sci. Adv.* **3**, e1602417 (2017).
36. J.-H. Na, A. A. Evans, J. Bae, M. C. Chiappelli, C. D. Santangelo, R. J. Lang, T. C. Hull, R. C. Hayward, Programming reversibly self-folding origami with micropatterned photo-crosslinkable polymer trilayers. *Adv. Mater.* **27**, 79–85 (2015).
37. J. T. B. Overvelde, T. A. de Jong, Y. Shevchenko, S. A. Becerra, G. M. Whitesides, J. C. Weaver, C. Hoberman, K. Bertoldi, A three-dimensional actuated origami-inspired transformable metamaterial with multiple degrees of freedom. *Nat. Commun.* **7**, 10929 (2016).
38. S. Kim, C. Laschi, B. Trimmer, Soft robotics: A bioinspired evolution in robotics. *Trends Biotechnol.* **31**, 287–294 (2013).
39. M. A. McEvoy, N. Correll, Materials that couple sensing, actuation, computation, and communication. *Science* **347**, 1261689 (2015).
40. J. Küpfer, H. Finkelmann, Nematic liquid single crystal elastomers. *Makromol. Chem. Rapid Commun.* **12**, 717–726 (1991).
41. S. W. Ula, N. A. Traugutt, R. H. Volpe, R. R. Patel, K. Yu, C. M. Yakacki, Liquid crystal elastomers: An introduction and review of emerging technologies. *Liq. Cryst. Rev.* **6**, 78–107 (2018).
42. T. Guin, B. A. Kowalski, R. Rao, A. D. Auguste, C. A. Grabowski, P. F. Lloyd, V. P. Tondiglia, B. Maruyama, R. A. Vaia, T. J. White, Electrical control of shape in voxelated liquid crystalline polymer nanocomposites. *ACS Appl. Mater. Interfaces* **10**, 1187–1194 (2018).
43. Y. Yao, J. T. Waters, A. V. Shneidman, J. Cui, X. Wang, N. K. Mandsberg, S. Li, A. C. Balazs, J. Aizenberg, Multiresponsive polymeric microstructures with encoded predetermined and self-regulated deformability. *Proc. Natl. Acad. Sci. U.S.A.* **115**, 12950–12955 (2018).
44. B. R. Donovan, V. M. Matavulj, S.-k. Ahn, T. Guin, T. J. White, All-Optical Control of Shape. *Adv. Mater.* **31**, 1805750 (2019).
45. T. H. Ware, M. E. McConney, J. J. Wie, V. P. Tondiglia, T. J. White, Voxelated liquid crystal elastomers. *Science* **347**, 982–984 (2015).
46. T. Guin, M. J. Settle, B. A. Kowalski, A. D. Auguste, R. V. Beblo, G. W. Reich, T. J. White, Layered liquid crystal elastomer actuators. *Nat. Commun.* **9**, 2531 (2018).
47. F. Greco, V. Domenici, A. Desii, E. Sinibaldi, B. Zupančič, B. Zalar, B. Mazzolai, V. Mattoli, Liquid single crystal elastomer/conducting polymer bilayer composite actuator: Modelling and experiments. *Soft Matter* **9**, 11405–11416 (2013).
48. A. Agrawal, T. Yun, S. L. Pesek, W. G. Chapman, R. Verduzco, Shape-responsive liquid crystal elastomer bilayers. *Soft Matter* **10**, 1411–1415 (2014).
49. P. Plucinsky, B. A. Kowalski, T. J. White, K. Bhattacharya, Patterning nonisometric origami in nematic elastomer sheets. *Soft Matter* **14**, 3127–3134 (2018).
50. H. Zeng, O. M. Wani, P. Wasylczyk, A. Priimagi, Light-driven, caterpillar-inspired miniature inching robot. *Macromol. Rapid Commun.* **39**, 1700224 (2018).
51. A. Kotikian, R. L. Truby, J. W. Boley, T. J. White, J. A. Lewis, 3D printing of liquid crystal elastomeric actuators with spatially programed nematic order. *Adv. Mater.* **30**, 1706164 (2018).
52. M. O. Saed, C. P. Ambulo, H. Kim, R. De, V. Raval, K. Searles, D. A. Siddiqui, J. M. O. Cue, M. C. Stefan, M. R. Shankar, T. H. Ware, Molecularly-engineered, 4D-printed liquid crystal elastomer actuators. *Adv. Funct. Mater.* **29**, 1806412 (2019).
53. C. P. Ambulo, J. J. Burroughs, J. M. Boothby, H. Kim, M. R. Shankar, T. H. Ware, Four-dimensional printing of liquid crystal elastomers. *ACS Appl. Mater. Interfaces* **9**, 37332–37339 (2017).

54. J. E. Smay, G. M. Gratson, R. F. Shepherd, J. Cesarano III, J. A. Lewis, Directed colloidal assembly of 3D periodic structures. *Adv. Mater.* **14**, 1279–1283 (2002).
55. M. López-Valdeolivas, D. Liu, D. J. Broer, C. Sánchez-Somolinos, 4D Printed Actuators with Soft-Robotic Functions. *Macromol. Rapid Commun.* **39**, 1700710 (2018).
56. N. P. Godman, B. A. Kowalski, A. D. Auguste, H. Koerner, T. J. White, Synthesis of elastomeric liquid crystalline polymer networks via chain transfer. *ACS Macro Lett.* **6**, 1290–1295 (2017).
57. S. Timoshenko, Analysis of Bi-Metal Thermostats. *J. Opt. Soc. Am.* **11**, 233 (1925).
58. P. Nardinocchi, E. Puntel, Unexpected hardening effects in bilayered gel beams. *Meccanica* **52**, 3471–3480 (2017).
59. V. Agostiniani, A. DeSimone, Dimension reduction via Γ-convergence for soft active materials. *Meccanica* **52**, 3457–3470 (2017).
60. S. D. Guest, S. Pellegrino, The folding of triangulated cylinders, part II: The folding process. *J. Appl. Mech.* **61**, 778–783 (1994).
61. R. J. Lang, *Twists, Tilings, and Tessellations* (CRC Press, 2018).
62. D. Rus, M. T. Tolley, Design, fabrication and control of soft robots. *Nature* **521**, 467–475 (2015).

Acknowledgments: We thank Y. Liu for experimental assistance and S. Uzel, W. Boley, K. Korner, P. Celli, S. Injeti, and H. Zhou for useful discussions. We thank L. K. Sanders for technical assistance with imaging and videography. **Funding:** The work was supported by the Army Research Office (ARO) Grant W911NF-17-1-0147 (to C.D. and C.M.), the Harvard MRSEC (NSF DMR-1420570 to J.A.L. and A.K.), and the ARO MURI Grant W911NF-17-1-0351 (to J.A.L. and E.C.D.). We also acknowledge support from the NASA Space Technology Research Fellowship to C.M. and the National Science Foundation Graduate Research Fellowship to A.K. This work made use of the Shared Experimental Facilities supported in part by the Harvard MRSEC Program under award number DMR-1420570. **Author contributions:** A.K., C.M., C.D., and J.A.L. conceived the concept and designed the experiments. A.K., C.M., E.C.D., and J.M.M. performed experiments. A.K., C.M., E.C.D., and R.D.W. analyzed data. A.K., E.C.D., J.M.M., and R.D.W. developed the printing system and testing environments. A.K., C.M., E.C.D., C.D., and J.A.L. wrote the paper. **Competing interests:** J.A.L. has cofounded a start-up company, Voxel8, which focuses on multimaterial 3D printing. **Data and materials availability:** All data needed to evaluate the conclusions in this paper are available in the paper or the Supplementary Materials.

Submitted 15 April 2019
Accepted 30 July 2019
Published 21 August 2019
10.1126/scirobotics.aax7044

Citation: A. Kotikian, C. McMahan, E. C. Davidson, J. M. Muhammad, R. D. Weeks, C. Daraio, J. A. Lewis, Untethered soft robotic matter with passive control of shape morphing and propulsion. *Sci. Robot.* **4**, eaax7044 (2019).

Science Robotics

Untethered soft robotic matter with passive control of shape morphing and propulsion

Arda Kotikian, Connor McMahan, Emily C. Davidson, Jalilah M. Muhammad, Robert D. Weeks, Chiara Daraio, and
Jennifer A. Lewis

Sci. Robot. **4** (33), eaax7044. DOI: 10.1126/scirobotics.aax7044

Science Robotics (ISSN 2470-9476) is published by the American Association for the Advancement of Science. 1200 New York Avenue NW, Washington, DC 20005. The title *Science Robotics* is a registered trademark of AAAS.